# Deformation Behavior and Failure Conditions in Pneumatic Bulge Forming Using Circular and Elliptical Dies

**Sabhan Hamid Ali**
Lecturer
University of Mosul
College of Engineering
Department of Mechanical Engineering
Iraq

**Anas Obeed Balod**
Assistant Professor
University of Mosul
College of Engineering
Department of Mechanical Engineering
Iraq

**Ataalah Hussain Jassim**
Professor
University of Mosul
College of Engineering
Department of Mechanical Engineering
Iraq

*The deformation and failure behavior of AA1050 aluminum sheet during warm pneumatic bulge forming (PBF) were investigated experimentally and numerically using circular and elliptical dies. The simulations were performed in Abaqus/Explicit using the Johnson–Cook (JC) model at 300 °C under constant pressure levels.*
*The results showed that the die aspect ratio has a strong effect on deformation and failure. The circular die led to more uniform biaxial deformation and high dome height, while elliptical dies caused non-uniform deformation and strain localization along the major axis. The failure occurred in the region of maximum thinning, where a crack extended along the major axis. The crack was small and located at the dome apex in the circular die, while in the elliptical dies, it became longer and more extended. The formability improved with increasing the sheet thickness (STH) from 0.7 mm to 1 mm, allowing higher strain and dome height before failure.*

***Keywords:*** *Pneumatic bulge forming, AA1050 aluminum, forming limit diagram, Die geometry, Sheet thickness, Fracture behavior.*

## 1. INTRODUCTION

The increasing demand to reduce fuel usage and envi–ronmental emissions in the industries of cars and aero–space has led to a wider use of lightweight materials, especially aluminum alloys, due to their good strength with respect to weight ratio. However, the formability of aluminum alloys at room temperature is still limited because of their low ductility and high springback, making it difficult to form complex shapes by using conventional methods. Therefore, a warm forming process has been developed, in which increasing the temperature, decreases flow stress, improves the duc–tility, and the thickness distribution. In addition, it inc–reases the height of the dome and decreases the forming pressure [1-3].

The bulge forming widely tackled the behavior of sheet metals under biaxial tensile stress, as it provides a more representative strain path compared to uniaxial ten–sile tests, and it allows higher plastic strain levels [4-6].

In the PBF, a gas pressure is used instead of a solid punch, as it has no contact between the tool and surface of the sheet, consequently, it reduces friction and leads to more uniform strain distribution. It also allows better control of the strain rate, making it suitable for studying the effects of temperature, pressure, and die geometry [7-9].

These advantages make PBF an attractive process for manufacturing lightweight sheet metal components with complex shapes. It can reduce the number of manufacturing operations, welding, and assembly steps, leading to lower production costs. Therefore, under–standing the effects of die geometry and STH on thic–kness distribution and failure behavior is essential for selecting suitable forming conditions for lightweight components used in automotive, aerospace, and marine applications [8,10-12].

Previous studies have supported the efficiency of this process. Hong et al. [13] showed that this process helps to draw Forming Limit Diagram (FLD) under elevated temperature and they distinguish between necking and fracture. Mitukiewicz et al. [5] highlighted the accuracy of this process in evaluating formability, while Hong et al. [8] reported that the pneumatic bulge test (PBT) improves the accuracy of the right-hand side of the FLD due to the absence of friction and its ability to stop at the onset of fracture. Paral and Mandal [6] reported that bulge tests can achieve higher plastic strain than tensile tests and give more information about the plasticity behavior. Lăzărescu et al. [4] revealed that this process is used to determine the curves of stress with strain under biaxial loading with good accuracy.

Concerning the failure prediction, Jebri et al. [14] showed that the JC model can successfully predict da–mage initiation and fracture under hydroforming vapor for the circular sheet of A1050. Nasri et al. [3] reported that strain distribution strongly affects the damage evolution for A1050 using levels of temperatures during comparative bulge and punch forming of the circular sheet. Whereas Hong et al. [8] confirmed that the temperature and strain rate affect failure mechanisms.

Temperature plays an important role in improving formability. Naeini et al. [2] mentioned that increasing the temperature increases the ductility, reduces flow

Received: May 2026, Accepted: July 2026
Correspondence to: Sabhan Hamid Ali,
University of Mosul, College of Engineering
Department of Mechanical Engineering, Iraq
E-mail: sabhanalrifaee@ntu.edu.iq
**doi: 10.5937/fme2603537H**

stress, and improves both dome height and thickness distribution during their investigation of Tube forming for AA1050 at different temperatures. Allazadeh [1] reported that increasing the temperature improves de–formation during his investigation of the A1050 alloy at different temperature and strain rates using tensile test. Sorgente et al. [15] explained that temperature controls the deformation mechanisms such as the cavitation and dislocation movement. Eladeb et al. [16] also stated that increasing temperature leads to reduce tearing and improving formability.

Pressure is the main factor that controls the defor–mation rate in the pneumatic forming. Cui et al. [7] showed that increasing pressure increases strain rate and dome height, but very high pressure may lead to early failure. Jiao et al. [12] reported that pressure affects the strain path, thickness distribution, and failure location, while Yi et al. [17] compared constant pressure with pressure–time controlled loading and showed that pressure path significantly affects thickness distribution and thinning during gas bulge forming..

Die aspect ratio also has a strong effect on the de–formation behavior. Hong et al. [8] showed that die shape affects the strain path and failure location. Giu–liano [18] explained that stress at the dome apex de–pends on the pressure, curvature radius, and STH.

Previous studies have reported different results reg–arding the effect of STH on the forming limit. Dilmec et al. [19] using the Nakajima and hydraulic bulge tests on AA2024-T4 aluminum alloy, found that increasing STH improved the forming limit. In contrast, Jiao et al. [12] using hydraulic bulge tests on 2A16-O aluminum alloy, reported that increasing STH only slightly increased the dome height, with no significant effect on the FLD.

Failure in bulge forming is mainly related to strain localization and damage accumulation under biaxial te–nsion. Most studies, such as Nasri et al. [3] Jiao et al. [12], and Hong et al. [8], reported that fracture usually occurs at the dome apex, although its location may be changed depending on temperature, pressure, and die geometry.

Although several studies have investigated pneu–matic bulge forming PBF, a review of the previous studies revealed several research gaps in this process. First, no previous study has investigated the combined effects of die aspect ratio and sheet thickness STH on thinning behavior and failure characteristics. Second, no previous study has established the FLD using more than one sheet thickness under different constant pressure levels. Finally, no validated numerical study has accu–rately predicted the failure location for dies with dif–ferent aspect ratios and multiple sheet thicknesses. These limitations motivated the present study. There–fore, this study develops and experimentally validates a finite element (FE) model capable of accurately predic–ting dome height, thickness distribution, forming limits, and failure location during PBF for dies with different aspect ratios.

Additionally, it provides new data on the FLD of AA1050 using more than one STH under different constant pressure levels. It also presents a compre–hensive evaluation of the effects of die aspect ratio and STH on thickness distribution and failure behavior and offers practical guidelines for selecting suitable forming conditions. Consequently, it contributes to reducing the experimental trials, manufacturing time, and production costs in PBF applications.

## 2. EXPERIMENTAL PROCEDURE

Commercially pure aluminum (AA1050) sheets with thickness of 1.0 and 0.7 mm were used in as received condition due to their wide industrial applications and good formability. The chemical composition is presented in Table 1. before testing the sheets were cut into 165 × 165 mm square specimens and cleaned.

To determine the mechanical properties of the material, uniaxial tensile tests were carried out at room temperature according to ASTM E8/E8M [20], as shown in Table 2. These properties were used for the calibration and validation of the Johnson Cook material model in the numerical analysis. The PBT were performed using a circular die with an inner diameter of 100 mm and elliptical dies with dimensions of (100 × 80 mm) and (100 × 40 mm), with an aspect ratio (AR) of 1, 0.8, and 0.4, respectively. All these dies were designed with a fillet radius of 5 mm, and they are made of steel as shown in Figure 1.

**Table 1. Chemical composition of AA1050 (wt.%)**

| Element | Value |
|---|---|
| Al | Rem. |
| Fe | 0.2 |
| Si | 0.15 |
| Cu | 0.015 |
| Mn | 0.01 |
| Ti | 0.02 |
| Zn | 0.01 |
| Mg | 0.055 |

**Table 2. Mechanical properties of AA1050 at 23 °C.**

| Mechanical properties | Value |
|---|---|
| Young's modulus (GPa) | 69 |
| Poisson's ratio | 0.33 |
| Yield strength (MPa) | 33 |
| Ultimat Strength (MPa) | 88 |
| Total Elongation (%) | 20 |

The sheet was clamped between the die and blank holder and this assembly was placed inside a laboratory furnace to reach the required temperature. The tempe–rature was measured using a K-type thermocouple (accuracy: ±2 °C) attached to the sheet, in addition to the furnace thermocouple.

Before applying the pressure and starting the for–ming process, the furnace was heated to the required temperature to ensure thermal stability. It was observed that the furnace temperature stabilized quickly, while the die and sheet required a long time to reach the target temperature due to gradual heat transfer.

Based on these observations, a thermal soak time of 10 minutes was applied to all experimental tests to en–sure full thermal equilibrium before loading. Figure 2(a) shows the overall experimental setup. After reaching thermal equilibrium, air pressure was applied using an air compressor. The pressure was controlled using an OMEGA PX309 pressure transducer (accuracy: ±0.25% full scale) and a proportional solenoid valve that were connected to a data acquisition system. The main components of the pneumatic pressure control system are illustrated in Figure 2(b).

Moreover, the data acquisition system was connected to a Linear Variable Differential Transformer (LVDT) with a linearity of less than ±0.2% full-scale output to measure the dome height. This setup allows real time for recording of pressure and height with time. Furthermore, the LVDT sensor was mounted on the top surface of the furnace to protect it from the heat, and displacement was transmitted to it through a ceramic rod that contacts with the sheet during deformation. A computer-based interface program was designed to display these curves in real time and to control the pressure path during the test, as shown in Figure 2(c). The sensor signals were analyzed using an Arduino system and LabVIEW software. The system automatically stops and shuts off the air supply when failure occurs. Details of the sensors and the proportional valve can be found in Refs. [21-23].

All experimental data (pressure, height, temperature, and time) were recorded in Excel files for further analysis and comparison with numerical results.

To ensure the accuracy of the experimental results, each test was repeated three times under identical testing conditions.

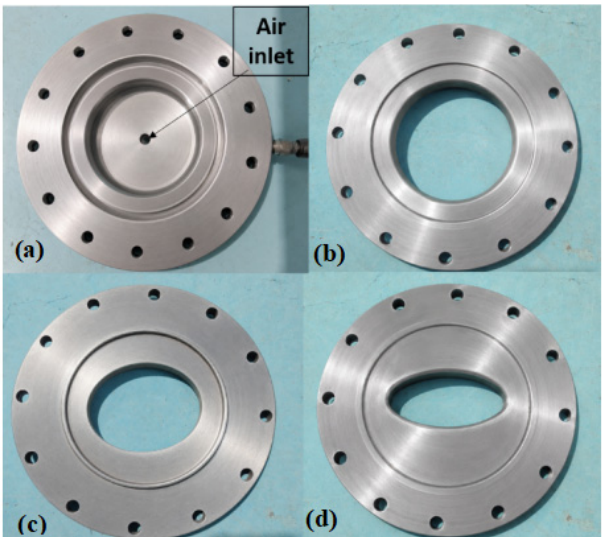


**Figure 1. Experimental tooling: (a) blank holder, (b) AR = 1.0, (c) AR = 0.8, and (d) AR = 0.4.**

For the strain measurement, circular grids with a diameter of 2 mm were applied on the sheet surface using fiber laser marking at a 300 mm/s, 50 Hz. This method provides a clear contrast without removing the material or affecting the mechanical behavior, and its thermal effect is negligible. This technique was adopted based on previous studies [24-27]. After the forming process, the circular grids were deformed into elliptical shapes due to the plastic deformation. The grids located in the fracture region, necking region, and safe region were selected according to the Hecker method [28].

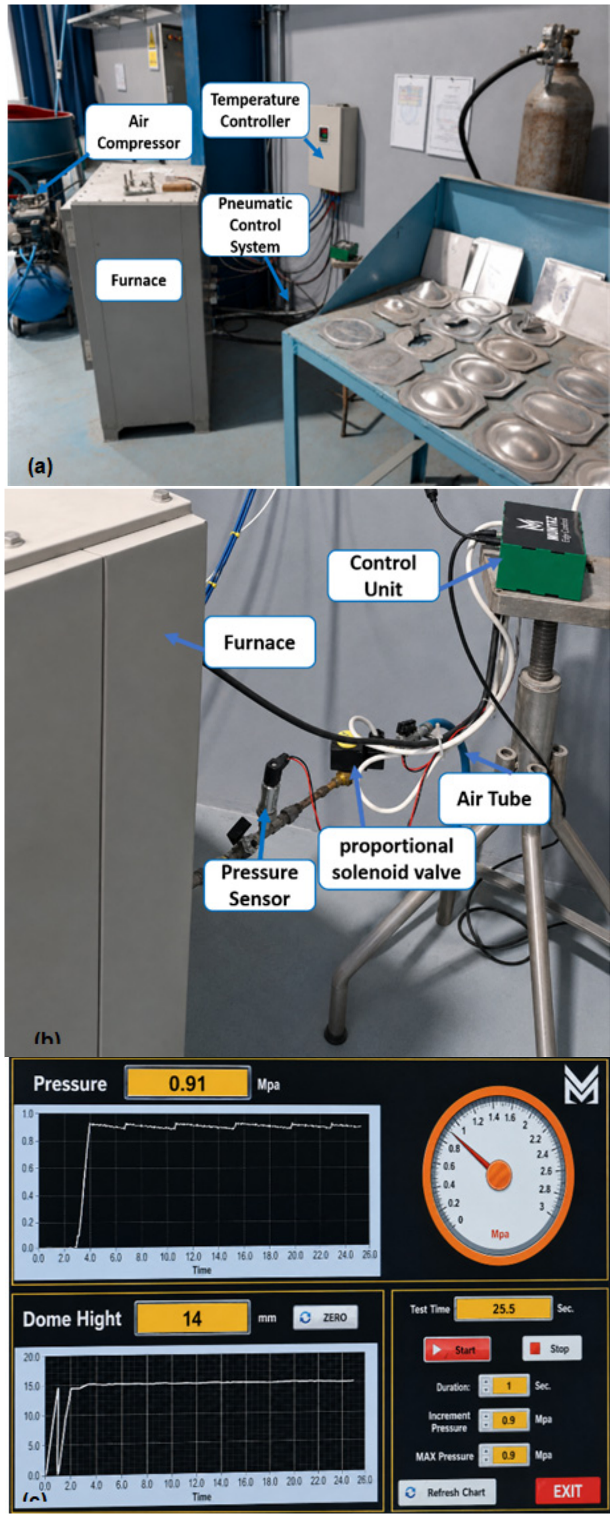


**Figure 2. Experimental setup and data acquisition system: (a) overall experimental setup in the laboratory, (b) pneumatic control system, and (c) LabVIEW-based monitoring and control interface.**

The deformed circles were measured using a Mitutoyo profile projector with a resolution of 0.001 mm to determine the major diameter $d_1$ and minor diameter $d_2$ as shown in Figure 3. The major ture strain ($\varepsilon_1$) and minor true strain ($\varepsilon_2$) were calculated using logarithmic strain equations according to ISO 12004-2 [29], as follows:

$$\varepsilon_1 = \ln\left(\frac{d_1}{d_0}\right) \tag{1}$$

$$\varepsilon_2 = \ln\left(\frac{d_2}{d_0}\right) \quad (2)$$

where $d_0$ is the initial circle diameter (2 mm), and $d_1$ and $d_2$ are the major and minor diameter after deformation. The calculated strain values were used to analyze the deformation behavior under biaxial tension.

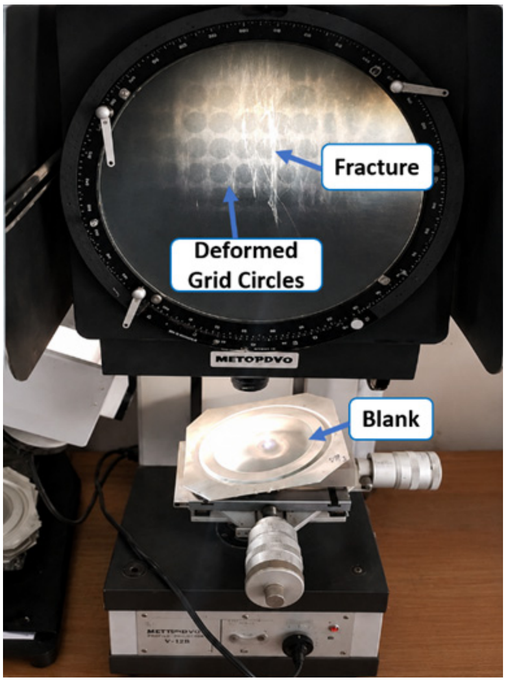


**Figure 2. Measurement of deformed grid circles using a profile projector.**

The thickness distribution was determined along the radial direction for the sheet, which was formed by the circular die, by measuring the thickness at different distances from the dome center to the edge. On the other hand, the thickness distribution for the sheet, which was formed by the elliptic die, was determined along the major axis, allowing accurate evaluation of the thinning behavior and determination of the minimum thickness location.

**Figure 3. Thickness Measurement Along Selected Points**

The thickness was measured by the destructive met–hod to deform the sheet and then using a digital vernier caliper (accuracy: ±0.02 mm), as shown in Figure 4. The thinning was calculated using (3):

$$\text{Thinning}(\%) = \frac{t_0 - t}{t_0} \times 100 \quad (3)$$

where ($t_0$) s the initial sheet thickness and (t) is the mea–sured thickness after forming. All measurements were taken at consistent radial distances to ensure accurate comparison with numerical results.

## 3. NUMERICAL MODEL

FE simulation has become an efficient tool for reducing experimental trials, optimizing tool geometry, and imp–roving process design in sheet metal forming processes [30]. Figure 5 shows that the geometry of circular and elliptical dies with different aspect ratios in the numerical model used to simulate the PBF process by using Abaqus/Explicit to reproduce the experimental conditions and validate the results accurately. The model consists of a deformable sheet, a rigid die, and a blank holder. The material properties were defined ac–cording to the data in Table 2, and the JC constitutive model was used to describe the material behavior, as it includes the strain hardening, strain rate sensitivity, and thermal effects. The flow stress is for this model exp–ressed as:

$$\sigma=\left(A+B\varepsilon_n^p\right)\left[1+C\ln\left(\frac{\dot{\varepsilon}_p}{\dot{\varepsilon}_0}\right)\right]\left[1-\left(\frac{T-T_0}{T_m-T_0}\right)^m\right] \quad (4)$$

where σ is the equivalent flow stress, A is the reference yield stress, B and n describe strain hardening behavior, and $\dot{\varepsilon}_p$ is the plastic strain rate normalized with respect to the reference strain rate $\dot{\varepsilon}_0$,The parameter C represents the sensitivity to strain rate, whereas $T_0$ and $T_m$ represents the room temperature and melting tempe–rature respectively. The parameter m is the thermal softening behavior of the material. [14,31]. The JC model constants used in this study, depending on the literature [3], after being compared with the tensile test results obtained in the present work, since these para–meters depend not only on chemical composition but also on the metallurgical condition and prior processing history, and these constants are shown in Table 3. Fur–thermore, the present study adopted the JC damage model that assumes that fracture occurs when the da–mage parameter D reaches a critical value of (D=1). The damaged element in the model will be removed from the calculation, according to the following relation:

$$D = \sum\left(\frac{\Delta\varepsilon_p}{\varepsilon_f}\right) \quad (5)$$

where $\Delta\varepsilon_p$ denotes the increment of accumulated plastic strain during each loading increment and $\varepsilon_f$ is the frac–ture strain, that can be expressed as:

$$\varepsilon_f=\left(D_1+d_2 d^{D_3\eta}\right)\left(1+D_4\ln\left(\frac{\dot{\varepsilon}}{\dot{\varepsilon}_0}\right)\right)\left(1+\frac{D_5\left(T-T_0\right)}{T_m-T_0}\right) \quad (6)$$

where $D_1$ define the reference strain, $D_2$ is the Expo–nential factor, $D_3$ is the control of stress triaxiality fac–

tor, $D_4$ represents the strain-rate sensitivity coefficient,, $D_5$ describes the temperature effect on damage evolu–tion, and η denotes the stress triaxiality [14].

The JC damage parameters adopted in this study were obtained from the literature [3] and are summari–zed in Table 4. A constant pressure was applied to the lower surface of the sheet to reproduce the experimental loading conditions, and contact interactions were defined using a surface-to-surface penalty formulation. The sheet edges were fully fixed to represent the clam–ping condition. Thermal conditions were assumed to be isothermal and were defined by applying a predefined temperature field on a sheet. The constant temperature 300 °C, was considered in the simulations to match the experimental conditions. The (FE) discretization and mesh configuration are shown in Figure 6. The sheet was modeled using S4R shell elements, where the ele–ment size was 0.8 mm. In addition, the final mesh con–sisted of 13,863 elements and 13,738 nodes, to maintain the accuracy of the results while achieving acceptable computational efficiency and solution time. The mesh convergence study was performed by testing different mesh densities. The results showed that further mesh refinement causes negligible changes in key outputs such as dome height and strain distribution.

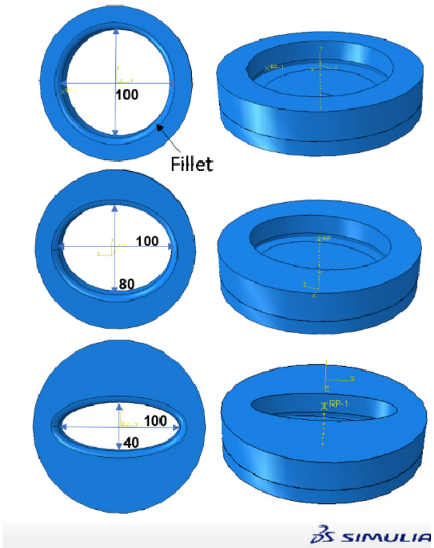


**Figure 4. Geometry of circular and elliptical dies with different aspect ratios.**

**Table 3. JC constitutive parameters used in the present study.**

| A(MPa) | B(MPa) | n | C | m | $T_m$ | $T_0$ |
|---|---|---|---|---|---|---|
| 32.504 | 132.06 | 0.435 | 0 | 1 | 658 | 23 |

**Table 4. The JC damage parameters adopted in this study.**

| $D_1$ | $D_2$ | $D_3$ | $D_4$ | $D_5$ |
|---|---|---|---|---|
| 0.558 | -0.05 | 0.62 | 0 | 0.477 |

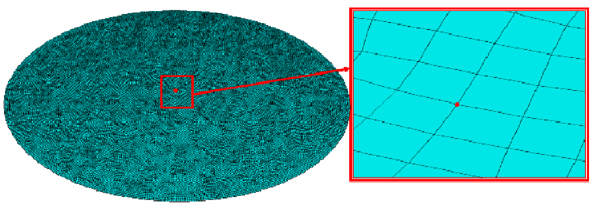

**Figure 6. FE mesh of the sheet model and enlarged view of the central mesh region.**

## 4. RESULTS AND DISCUSSION

### 4.1 Effect of Die Aspect Ratio

#### 4.1.1 Effect of Die Aspect Ratio on Pressure

Die geometry has a direct effect on the forming beha–vior during the bulge forming process. The results sho–wed that elliptical dies require higher pressure compared to the circular die to keep similar forming conditions. This is due to the higher geometric constraint in elliptical dies, which limits material flow and reduces the formability.

As shown in Figure 7, increasing the constant pres–sure level reduces the time to failure for all dies. In contrast, decreasing the aspect ratio (AR) leads to a sig–nificant increase in forming time when compared under the same constant pressure level, especially at low pres–sures. This is because the strain distribution in elliptical dies is less uniform than in the circular die. Therefore, to ensure similar forming conditions in elliptical dies, either higher pressure or longer forming time is required, under the same operating conditions of this study, such as tem–perature, STH, and other process parameters.

The results of this study also correspond with pre–vious studies, which reported that applying constant pressure does not produce a constant strain rate, but it is changed over time due to the evolution of the dome shape and the changing geometry of the deformation region. In some of the subsequent sections of this study, the mean equivalent strain rate is used as a comparison parameter based on different constant pressure levels, as will be explained later. It was calculated using (7):

$$\overline{\varepsilon}' = \frac{1}{t_f}\int_0^{t_f} \varepsilon'(t)\,dt \approx \frac{1}{t_f}\sum_{t=0}^{t=t_f} \varepsilon'(t)\,\Delta t \qquad (7)$$

where $t_f$ is the time necessary to reach a target strain value, ε`(t) represents the equivalent strain rate as a fun–ction of time, The quantities dt and Δt indicate diffe–rential and finite time intervals, respectively [15,32, 33].

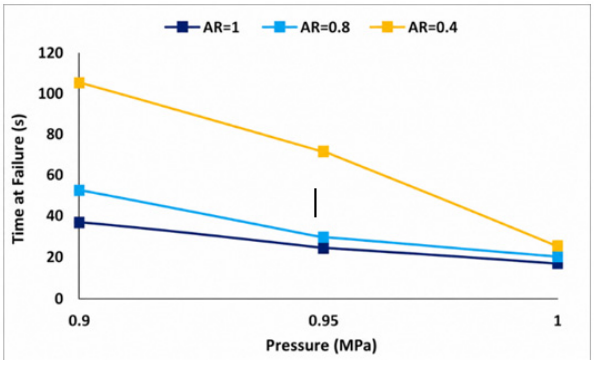


**Figure 5. Effect of Die Aspect Ratios on Constant Pressure Levels vs. Time at Failure of A1050 at 300 °C with 1 mm.**

#### 4.1.2 Effect of Die Aspect Ratio on Dome Height

Figure 8 shows the evolution of dome height with time for both the experimental and numerical results under the temperature of 300 °C and a constant pressure of 0.9 MPa for dies with different aspect ratios (AR = 1, 0.8, 0.4). The circular die (AR = 1) showed the highest final dome height, while the die (AR = 0.4) recorded the lowest dome height with the longest forming time.

This behavior can be explained by stating that the circular die provides a more uniform biaxial tensile state due to its full geometric symmetry. Allowing stress and strain to be distributed more uniform over the sheet surface and delaying local deformation concentration. Therefore, the highest formability and the greatest final dome height were obtained.

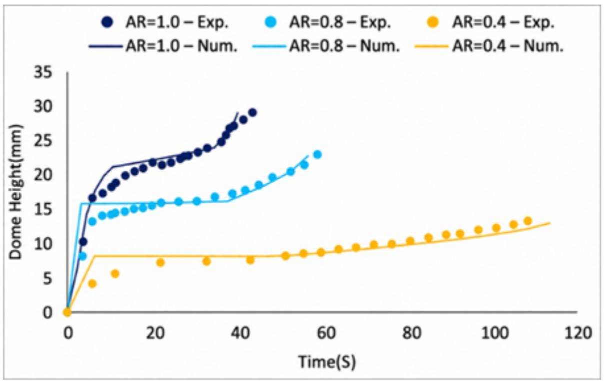


**Figure 6. Dome Height vs Time for Different Die Aspect Ratios at 1 mm Thickness, 300 °C, and 0.9 MPa**

The triaxiality results in Figure 9 support this beha–vior, as the values remained close to the balanced bia–xial tension state during most stages of deformation. Whereas in the elliptical dies, reducing the aspect ratio led to increase the difference between the two main axes. Thus, the deformation conditions became nonuni–form in the longitudinal and transverse directions. This geometric difference gradually changes the strain path from a uniform biaxial tension state toward a condition closer to plane strain along the minor axis, with greater material flow toward the major axis. Therefore, the die (AR = 0.8) showed only a limited reduction in dome height, because it still maintained a good level of biaxial deformation, while at (AR = 0.4) the reduced triaxiality value led to a larger deviation in the strain path that led to obtain lower final dome height.

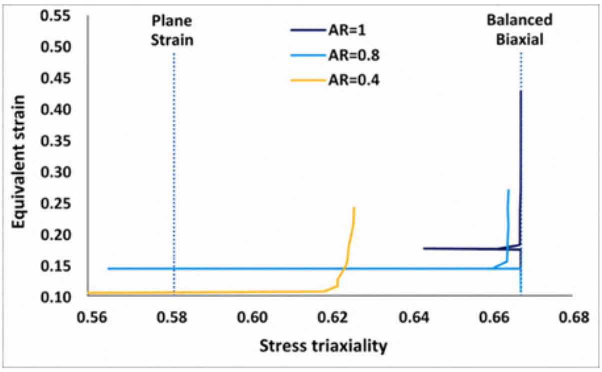


**Figure 7. Evolution of stress triaxiality versus equivalent strain for different die aspect ratios at 1 mm Thickness, 300 °C, and 0.9 MPa.**

Figure 10 shows that the strain rate changes over time and is affected by the dome shape evolution and the die geometry during the forming process. It can be seen that the strain rate was the highest in the circular die, then it was decreased as the aspect ratio was reduced to 0.8 and then 0.4. Moreover, the shortest forming time was obtained in the circular die due to the higher deformation rate and dome expansion into the die cavity. While the forming time increased slightly for (AR = 0.8), but the longest forming time was recorded for (AR = 0.4) because of the lower strain rate and the limited material flow, which led to lower dome growth. It can also be observed from the figure that all curves pass through three main stages. In the first stage, the strain rate is relatively high at the beginning of the forming process due to the rapid response of the sheet to the applied pressure. Whereas in the second stage, the strain rate decreases, indicating more stable and gradual deformation. In the third stage, the strain rate increases suddenly, which indicates the onset of localized necking and accelerated to failure.

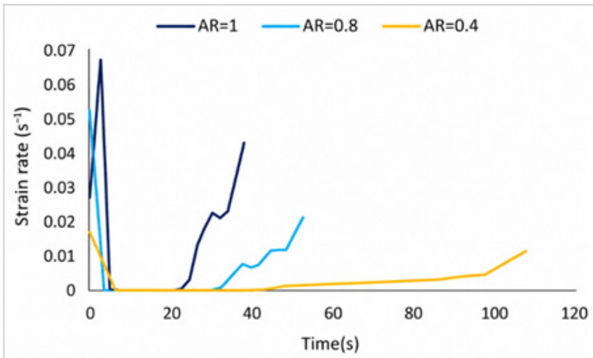


**Figure 8. Strain Rate vs Time for Different Die Aspect Ratios at 1 mm Thickness, 300 °C, and 0.9 MPa.**

### 4.1.3 Effect of Die Aspect Ratio on Thinning Distribution and Fracture Behavior

The equivalent plastic strain (PEEQ) contours in Figure 11 showed that the circular die (AR =1) produced a more uniform and axisymmetric strain distribution around the dome apex, while the distribution became more elongated for (AR = 0.8) and more concentrate for (AR = 0.4). This indicates that the deformation is chan–ged from a distributed mode to a more localized mode with decreasing the aspect ratio. It was also observed that the highest plastic strain values were concentrated at the dome apex.

Although the PEEQ contours in Figure 11 show a tendency to strain localization with decreasing the aspect ratio, the thinning results in Figure 12, that were measured along the major axis, show that the lowest thinning occurred at the elliptical die (AR = 0.4), while the highest values are observed in the circular die (AR = 1). This is because deformation in elliptical dies is non-axisymmetric, with strain concentrating along the major axis. This die geometry leads to localized thinning along the major axis. However, the overall thinning remains lower than in the circular die.

The thinning results are in good agreement with the PEEQ distribution observed in Figures 11 and 12 as the circular die allows more stable and uniform deformation, resulting in a greater dome height, higher plastic strain accumulation, and thus higher thinning. In contrast, the low aspect ratio elliptical die limits deformation development, thus, this causes the strain to localize within limited regions.

Figure 13 shows a small crack at the center of the dome apex for the circular die (AR = 1), while at (AR = 0.8) the failure develops into irregular elongated crack.

Whereas at (AR = 0.4), the crack becomes longer and extends along the major axis. A good agreement between the numerical and experimental results is also observed in pictures of both the location and shape of failure.

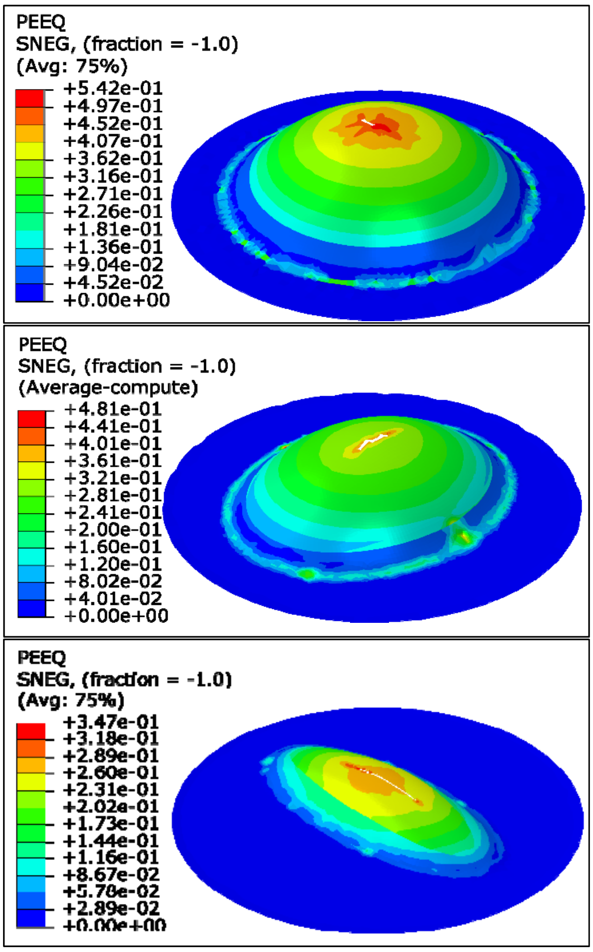


**Figure 11. Comparison of PEEQ Distribution for Different Die Aspect Ratios at 1 mm Thickness, 300 °C, and 0.9 MPa.**

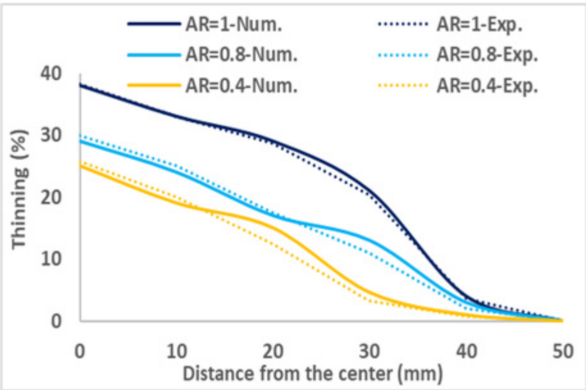


**Figure 9. Experimental and Numerical Thinning Distribution along the Major Axis at 1 mm Thickness, 300 °C, and 0.9 MPa for Different Die Aspect Ratios**

To explain the cause of the fracture along the major axis in elliptical dies, Figure 14 shows the thickness distribution STH for different die aspect ratios. It can be observed that the minimum thickness occurs along the major axis, indicated by the blue region, particularly near the crack boundary for each case. This confirms that fracture takes place in the direction of the maximum thinning, as a result of strain localization and non-uniform deformation in elliptical dies.

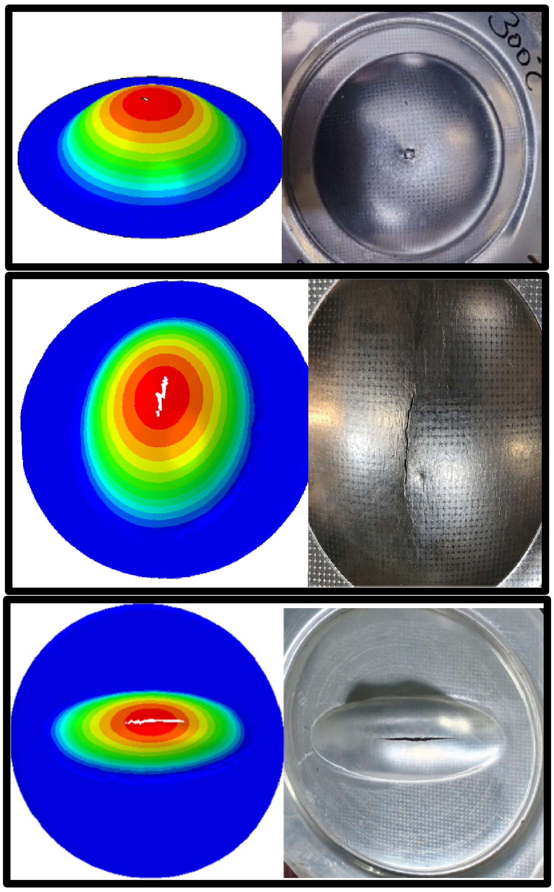

**Figure 13. Experimental and Numerical Fracture Morphology for Different Die Aspect Ratios at 1 mm Thickness, 300 °C, and 0.9 MPa.**

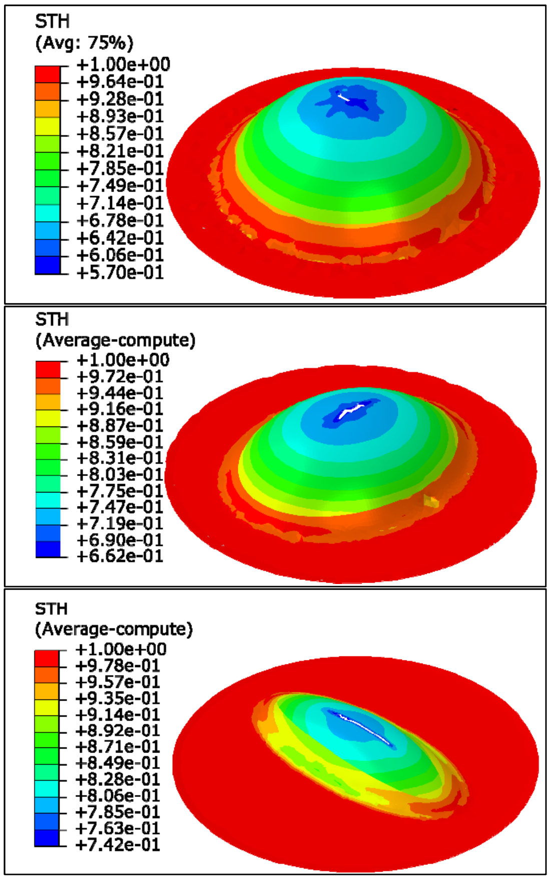


**Figure 14. Thickness Distribution at the Fracture Edge for Different Die Aspect Ratios at 1 mm Thickness, 300 °C, and 0.9 MPa.**

### 4.1.4 Validation of the Numerical Results under Different Die Aspect Ratios

Figures 8, 12, and 13 demonstrate good agreement bet– ween the experimental and numerical results for AA1050 sheets with a thickness of 1 mm formed at 300 °C under a constant pressure of 0.9 MPa using different die aspect ratios. Table 5 summarizes the statistical comparison of the final dome height and maximum thinning at fracture. The experimental values are reported as the mean ± standard deviation (SD) obtained from repeated tests. The percentage errors between the experimental and nume– rical results were below 4% for all die aspect ratios. Furthermore, the expanded measurement uncertainty was estimated to be less than ±0.7 mm for the dome height and ±3.0% for the maximum thinning.

**Table 5. Statistical comparison of the final experimental and numerical results at fracture under 0.9 MPa and 300 °C.**

| AR | 1.0 | 0.8 | 0.4 |
|---|---|---|---|
| Exp. dome height (Mean ± SD), mm | 28.60 ± 0.55 | 22.00 ± 0.45 | 12.01 ± 0.25 |
| Num. dome height, mm | 28.10 | 21.60 | 11.70 |
| Height error (%) | 1.75 | 1.82 | 2.58 |
| Exp. max thinning (Mean ± SD), % | 25.0 ± 0.50 | 29.0 ± 0.60 | 38.0 ± 0.80 |
| Num. max thinning, | 25.8 | 30.0 | 38.2 |
| Thinning error (%) | 3.20 | 3.45 | 0.53 |

## 4.2 Effect of STH

### 4.2.1 Effect of STH on Pressure

To study the effect of STH on dome height and thinning behavior, AA1050 sheets with thicknesses of 1 mm and 0.7 mm were tested under a constant pressure of 0.9 MPa, the sheet of 0.7 mm with the circular die (AR = 1) failed in less than 5 s as in Figure 15, while the sheet of 1 mm was successfully formed for all die aspect ratios. At lower pressure levels, the 1 mm sheets require more than 600 s, which was the maximum planned test time. Therefore, a direct comparison at one pressure level was not possible.

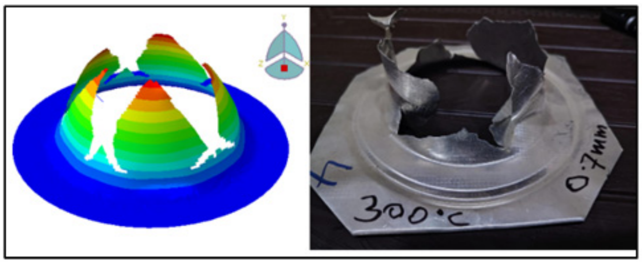


**Figure 10. Rupture Behavior at 300 °C and 0.9 MPa for AA1050 (t = 0.7 mm).**

Therefore, the comparison between both thicknesses and all die shapes was carried out based on a similar mean equivalent strain rate under different constant pre– ssure levels. The equivalent strain was obtained directly from the PEEQ variable in Abaqus, and it was also calculated from the principal strains using the von Mises relation. Both methods showed a good agreement. After that, the mean equivalent strain rate until failure was calculated by using (7).

The experiments were performed over a range of constant pressure levels from (0.5 to 1 MPa). The results showed that the mean equivalent strain rate va– lues for the selected levels were very close, as illustrated in Figure 16, with values approximately $\overline{\varepsilon}' \approx 0.01 \pm 0.001 s^{-1}$, thus, an approximate value of $\overline{\varepsilon}' \approx 0.01 s^{-1}$ was used. This confirms that the comparison between the two thicknesses and the different dies was carried out under similar strain rate conditions, making the comparison more objective for evaluating the effect of STH and die geometry on formability.

Figure 16 shows that increasing the STH from 0.7 to 1 mm required a higher constant pressure to reach a similar mean strain rate 0.01 s□$^{1}$. The required pressure increased by 42.86% to 50%, depending on the die as– pect ratio, indicating the greater deformation resistance of the thicker sheets.

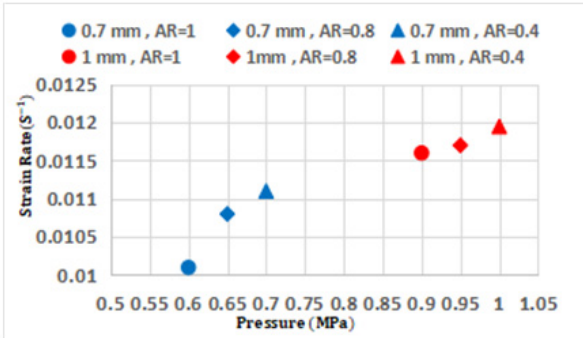


**Figure 11. Relationship Between Pressure and Mean Strain Rate for Selected Pressure Levels at Different Thicknesses and Die Aspect Ratios.**

### 4.2.2 Effect of STH on Dome Height

Increasing the STH from 0.7 to 1 mm led to a higher dome height at failure for all die aspect ratios, as shown in Figure 17. The increase reached 11.14% at AR = 1, 4.40% at AR = 0.8, and 3.20% at AR = 0.4. It can be observed that the effect of thickness was clearer in the circular die, then it gradually decreases with decreasing the aspect ratio. This behavior may be resulting from the higher deformation capacity of thicker sheets, which allows the material to maintain larger plastic deforma– tion before failure. This is also supported by the PEEQ results, as in Figure 18, which shows higher accumu– lated plastic strain in the thicker sheet compared to the thinner sheet.

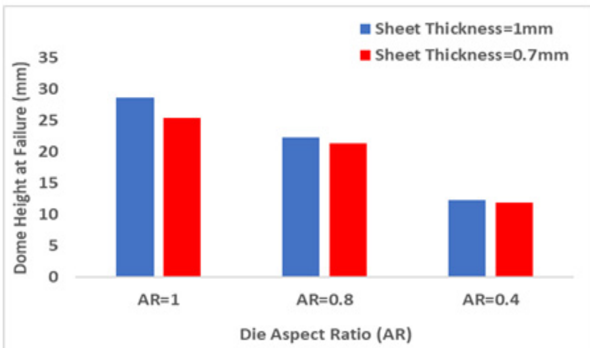


**Figure 12. Experimental effect of (STH) on Dome Height at Failure at 300 °C and 0.01 $s^{-1}$.**

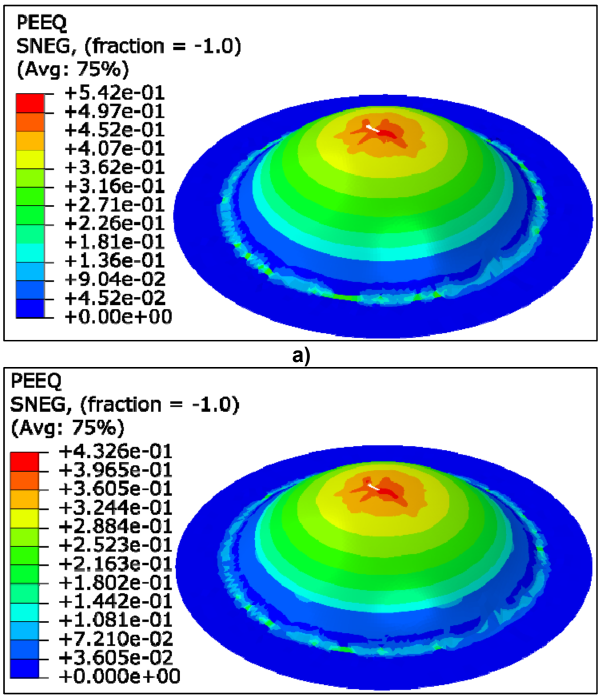


**Figure 18. Effect of STH on the PEEQ Distribution: (a) 1 mm and (b) 0.7 mm.**

### 4.2.3 Effect of STH on Thinning

Figure 19 shows the distribution of thinning along the radial path. The thinning reaches its maximum value at the dome apex and then gradually decreases toward the die edge. It can also be observed that increasing the STH from 0.7 to 1 mm leads to a higher final thinning level, especially at the apex. This indicates that the thicker sheet can undergo larger plastic deformation before failure due to delayed strain localization, delayed necking, and improved deformation stability. As a result, this behavior directly appears in the increased dome height, as shown in Figure 17, where the longer biaxial stretching allows a higher dome height to be reached before failure. This analysis is supported by Figure 20, where the minimum thickness is located at the dome apex for both sheet thicknesses. The thinning distribution is very similar in both cases, indicating that the location and shape of the fracture are not affected by the STH, and the effect of thickness is mainly on the amount of thinning.

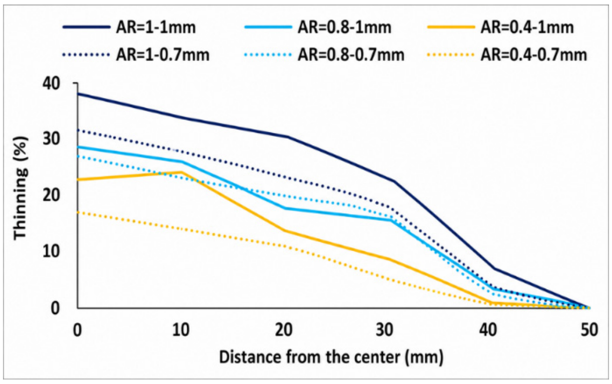


**Figure 19. Experimental thinning distribution along the major axis for 1 mm and 0.7 mm AA1050 sheets at 300 °C and a mean strain rate of 0.01 s$^{-1}$.**

In addition, the thickness distribution from the apex to the edge appears more gradual in the thicker sheet, showing more stable deformation behavior. Further–more, a very good agreement between the experimental and numerical results is observed in terms of thickness distribution and the location of minimum thickness, confirming the accuracy of the numerical model.

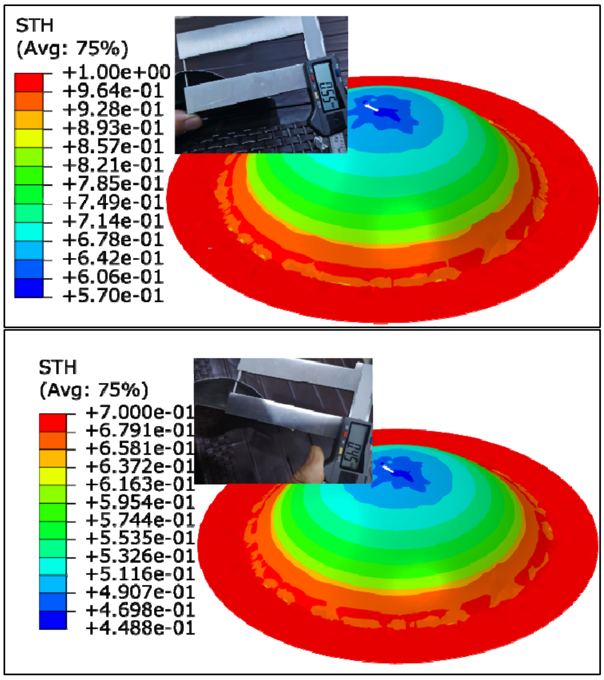


**Figure 20. Experimental and Numerical Thickness Distribution for 1 mm and 0.7 mm Sheets.**

### 4.2.4 Validation of the Numerical Results under Dif–ferent Sheet Thicknesses and Die Aspect Ratios

Figure 20 compares the experimental final thickness at the dome apex with the numerical thickness contours for AA1050 sheets with thicknesses of 1 and 0.7 mm. Good agreement is observed between the experimental and numerical final thicknesses at the dome apex for both sheet thicknesses. The numerical results were not superimposed on Figures 17 and 19 to maintain figure clarity. Instead, Table 6 summarizes the statistical com–parison of the final dome height and maximum thinning at fracture, including the experimental mean ± standard deviation (SD) obtained from repeated tests and the percentage errors between the experimental and nume–rical results were below 3% for all sheet thick–nesses. Furthermore, the expanded measurement uncertainty was estimated to be less than ±0.7 mm for the dome height and less than ±4.5% for the maximum thinning.

**Table 6. Statistical comparison of the final experimental and numerical results at fracture for different sheet thicknesses and die aspect ratios at 300 °C and mean strain rate of 0.01 s-1.**

| Thickness (mm) | Parameter | AR = 1.0 | AR = 0.8 | AR = 0.4 |
|---|---|---|---|---|
| 1.0 | Exp. dome height (Mean ± SD), mm | 28.60 ± 0.55 | 22.30 ± 0.45 | 12.24 ± 0.25 |
| | Num. dome height, mm | 28.10 | 21.80 | 11.90 |

| | | | | |
|---|---|---|---|---|
| | Height error (%) | 1.75 | 2.24 | 2.78 |
| | Exp. max thinning (Mean ± SD), % | 23.00 ± 0.50 | 29.00 ± 0.60 | 38.00 ± 0.80 |
| | Num. max thinning, % | 23.60 | 29.80 | 37.20 |
| | Thinning error (%) | 2.61 | 2.76 | 2.11 |
| 0.7 | Exp. dome height (Mean ± SD), mm | 25.43 ± 0.50 | 21.36 ± 0.40 | 11.86 ± 0.25 |
| | Num. dome height, mm | 24.90 | 20.90 | 11.55 |
| | Height error (%) | 2.08 | 2.15 | 2.61 |
| | Exp. max thinning (Mean ± SD), % | 31.43 ± 0.65 | 27.14 ± 0.55 | 17.14 ± 0.40 |
| | Num. max thinning, % | 30.80 | 27.80 | 17.60 |
| | Thinning error (%) | 2.00 | 2.43 | 2.68 |

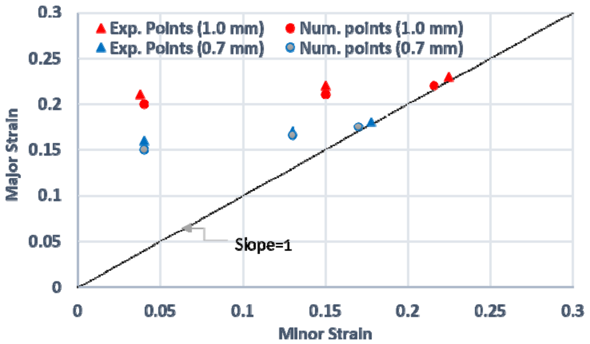


**Figure 21. FLD in the Biaxial Region for AA1050 at 300°C and 0.01 $s^{-1}$(0.7 and 1 mm).**

### 4.2.5 Effect of STH on the FLD

As shown in the previous sections, increasing the STH led to higher dome height at failure, with different percentages depending on the die aspect ratio. This is also associated with increasing of thinning, especially at the dome apex. To verify that this behavior represents a real improvement in formability, the forming limit of the material was evaluated under the same test conditions. Therefore, the FLD for AA1050 aluminium alloy was established using the same dies and loading conditions used in the previous section. Figure 21 shows the right side of the FLD under biaxial tensile conditions resulting from the pneumatic bulging process, where all points lie in the tension–tension region. The strain points were obtained using three dies with different aspect ratios, with each point representing a different strain state at failure. To ensure the reliability of the results, an uncertainty analysis was performed for the major and minor strains. The expanded uncertainty was ±0.0008, which is very small compared with the differences between the forming limit points. This confirms that the observed differences are due to the sheet thickness rather than measurement uncertainty. It can be observed that increasing the thickness from 0.7 to 1 mm leads to higher major strain values at the same minor strain levels, with a tendency toward balanced biaxial stretching. This indicates a better formability and a higher forming limit.

These results agree with previous studies about other materials [19], which reported that increasing thickness increases the forming limit and dome height. However, they differ from the findings of [12], which reported that STH has no significant effect on the FLD.

The increase in the forming limit observed in the present study indicates that the thicker sheet can withstand greater plastic deformation before failure. This behavior is linked with increasing deformation stability and delaying strain localization and necking. Thus, it can be concluded that increasing STH improves the forming limit and allows the sheet to reach higher strain levels before failure without changing the main failure mechanism.

## 5. CONCLUSIONS

The study concludes the following:

The die aspect ratio has a strong effect on the forming behavior. The circular die provides the best strain distribution and highest deformation stability, leading to the highest dome height and plastic strain. In contrast, decreasing the aspect ratio (AR) leads to reduce the dome height and strain levels.

The failure is affected by the die aspect ratio in the circular die, the crack is small and centred at the apex, while in elliptical dies, it becomes longer and extends along the major axis in the region of maximum thinning.

The location and general shape of failure are not affected by increasing STH, as the failure behavior remains similar in all cases.

Increasing STH improves the formability by increasing dome height and allowing higher strain levels before failure. This is associated with higher thinning, which improves deformation stability and delays strain localization and necking.

To maintain the same strain rate, higher pressure is required when decreasing the aspect ratio of dies or increasing the STH.

Forming can be performed at the same constant pressure by increasing forming time, which leads to a lower strain rate.

Increasing thickness raises the forming limit in the biaxial region, allowing higher strain levels.

A good agreement was observed between experi–mental and numerical results.


## ACKNOWLEDGMENT

The authors would like to express their heartfelt thanks to Northern Technical University/Mosul Polytechnic Col–lege/Mechanical Department for providing the facilities and support necessary to carry out this research.


## REFERENCES


[1] Allazadeh, M.R.: Computing Strain Rate Sensiti–vity of Aluminium Alloy 1050, International Scien–tific Survey Journal, Vol. 3, No. 2, pp. 9-19, 2020.

[2] Naeini, H.M., Liaghat, G.H., Hashemi Ghiri, S.J. and Seyedkashi, S.M.H.: FE Simulation and Expe–rimental Study of Tube Hydroforming Process for AA1050 Alloy at Various Temperatures, Advanced Materials Research, Vol. 264-265, pp. 96-101, 2011.

[3] Nasri, M.T., Abbassi, F., Ahmad, F., Makhloufi, W., Ayadi, M., Mehboob, H. and Choi, H.S.: Experimental and Numerical Investigation of Sheet Metal Failure Based on Johnson-Cook Model and Erichsen Test over a Wide Range of Temperatures, Mechanics of Advanced Materials and Structures, Vol. 30, No. 10, pp. 2087-2100, 2023.

[4] Lăzărescu, L., Comşa, D.-S., Nicodim, I., Ciobanu, I., Banabic, D.: Characterization of Plastic Behaviour of Sheet Metals by Hydraulic Bulge Test, Transactions of Nonferrous Metals Society of China, Vol. 22, Suppl. 3, pp. S275-S279, 2012.

[5] Mitukiewicz, G., Anantheshwara, K., Zhou, G., Mishra, R.K. and Jain, M.K.: A New Method of Determining Forming Limit Diagram for Sheet Materials by Gas Blow Forming, Journal of Materials Processing Technology, Vol. 214, No. 12, pp. 2960-2970, 2014.

[6] Paral, S.K. and Mandal, A.: An Experimental Study on Bulge Test of Commercially Pure Aluminium Sheet Metal, Journal of the Institution of Engineers (India): Series D, Vol. 104, No. 1, pp. 37-43, 2023.

[7] Cui, X., Yang, G., Yan, Z., Chen, X., Wang, H. and Huang, C.: Enhanced Forming Height and Accuracy of Thin-Walled Aluminum Alloy by Impact Pneumatic Forming, Journal of Materials Processing Technology, Vol. 330, Article No. 118456, 2024.

[8] Hong, J.-H., Yoo, D., Kwon, Y.N. and Kim, D.: Pneumatic Experimental Design for Strain Rate Sensitive Forming Limit Evaluation of 7075 Aluminum Alloy Sheets under Biaxial Stretching Modes at Elevated Temperature, Metals, Vol. 10, No. 12, Article No. 1639, 2020.

[9] Li, B., Hu, Z., Xie, Y. and Wang, Y.: Investigation on Deformation Behavior and Microstructure of AZ31B Alloy within Hot Gas Bulging with Clustering Balls, Journal of Alloys and Compounds, Vol. 1031, Article No. 180980, 2025.

[10] Falk, C.: Hot Metal Gas Forming of Aluminium for Automotive, Shapes by Hydro. Available at: https://www.shapesbyhydro.com/en/knowledge/hot-metal-gas-forming-of-aluminium-for-automotive/ (Accessed: May 29, 2026).

[11] Chen, Y., Zhao, S., Wang, Y., Liu, Y., Hu, Z., Qian, D., Han, X., Wang, H., Lin, J. and Hua, L.: Advanced Forming Technologies for Integrated Metal Components with Extreme Size and Structure: State-of-the-Art and Perspectives, Chinese Journal of Mechanical Engineering, Vol. 39, Article No. 100027, 2026.

[12] Jiao, Z., Li, Y., Jiang, P., Li, K. and Lang, L.: The Forming Limit Diagram of 2A16 Aluminum Alloy Sheet Based on Hydraulic Bulging Test of Elliptical Die, MATEC Web of Conferences, Vol. 401, Paper No. 03003, 2024.

[13] Hong, J.-H., Yoo, D., Kwon, Y.N., Kim, D.: Evaluation of Rate-Dependent Forming Limit for AA7075 Sheets under Pneumatic Stretching Method at Elevated Temperatures, Journal of Materials Research and Technology, Vol. 22, pp. 1839-1854, 2023.

[14] Jebri, L., Lazghab, T., Toumi, M. and Soula, M.: The Behavior and Forming Performance of Vapor Hydroforming Process of Thin Aluminum Sheets: Numerical and Experimental Analysis, Advances in Mechanical Engineering, Vol. 14, No. 4, 2022.

[15] Sorgente, D., Palumbo, G., Scintilla, L.D., Tricarico, L.: Gas Forming of an AZ31 Magnesium Alloy at Elevated Strain Rates, International Journal of Advanced Manufacturing Technology, Vol. 83, Nos. 5-8, pp. 861-872, 2016.

[16] Eladeb, A., Nasri, M.T., Becheikh, N., Ghazouani, N. and Tashkandi, M.A.: Study on the Thermal Sensitivity of Anisotropic Thin Sheets: Application to Hot Bulge Tests, Mechanika, Vol. 30, No. 2, pp. 110-122, 2024.

[17] Yi, L., Gu, Z., Li, Y. and Sun, G.: A Study on Superplastic Gas Bulging Forming Process of Industrial 5083 Aluminum Alloy, Materials Today Communications, Vol. 50, Article No. 114361, 2026.

[18] Giuliano, G.: Thickness and Strain Rate at the Sheet Dome Apex in Superplastic Bulge Forming Tests, International Journal of Material Forming, Vol. 2, Suppl. 1, pp. 375-378, 2009.

[19] Dilmec, M., Halkaci, H.S., Ozturk, F., Livatyali, H. and Yigit, O.: Effects of Sheet Thickness and Anisotropy on Forming Limit Curves of AA2024-T4, International Journal of Advanced Manufacturing Technology, Vol. 67, Nos. 9-12, pp. 2689-2700, 2013.

[20] ASTM International: ASTM E8/E8M-13a: Standard Test Methods for Tension Testing of Metallic Materials, ASTM International, West Conshohocken, PA, 2013.

[21] Omega Engineering: Stainless Steel Pressure Transducers – PX309 Series. Available at: https://www.dwyeromega.com/en-us/general-purpose-stainless-steel-pressure-transducers/p/PX309 (Accessed: February 15, 2026).

[22] Tameson: Proportional Solenoid Valves. https://tameson.com/collections/proportional-solenoid-valves (Accessed: February 15, 2026).

[23] Omega Engineering: AC and DC LVDTs. https://www.omega.co.uk/subsection/dc-lvdt-sensors.html (Accessed: February 15, 2026).

[24] Kumar, S., Ethiraj, N., Sivabalan, T., Farhan, M. and Bernadette, T.: Investigation on Component Wall Angle in Single Stage Incremental Forming of Austenitic Stainless Steel AISI 304 Sheet, FME Transactions, Vol. 48, No. 2, pp. 391-396, 2020.

[25] Mäntyjärvi, K., Tulonen, J., Saarnivuo, T., Porter, J., Karjalainen, J.A.: Grid Patterns by Laser for Forming Strain Analysis, International Journal of Material Forming, Vol. 1, Suppl. 1, pp. 249-252, 2008.

[26] Yi, S., Hyun, D., Hong, S.: Tensile Specimen Circular Grid Pattern and AI-Based Strain Calculation Method, Preprints, Article No. 2024072393, 2024.

[27] Yildiz, R.A., Yilmaz, S.: The Verification of Stra–ins Obtained by Grid Measurements Using Digital Image Processing for Sheet Metal Formability, Journal of Strain Analysis for Engineering Design, Vol. 52, No. 8, pp. 506-514, 2017.

[28] Hecker, S.S.: A Simple rve Technique and Results on Aluminum Alloys, in: Sheet Metal Forming and Formability, Proceedings of the Sheet Metal For–ming and Formability Conference, Amsterdam, The Netherlands, pp. 51-58, 1972.

[29] International Organization for Standardization: ISO 12004-2:2021, Metallic Materials – Sheet and Strip – Determination of Forming-Limit Curves – Part 2: Determination of Forming-Limit Curves in the Laboratory, ISO, Geneva, Switzerland, 2021.

[30] Benisa, M., Babic, B., Grbovic, A., Stefanovic, Z.: Numerical Simulation as a Tool for Optimizing Tool Geometry for Rubber Pad Forming Process, FME Transactions, Vol. 42, No. 1, pp. 67-73, 2014.

[31] Chtioui, A., Ouballouch, A. and Mouchtachi, A.: Investigation of Cutting Responses During High-Speed Machining of Ti6Al4V Alloy: Finite Ele–ment Analysis, FME Transactions, Vol. 52, No. 4, pp. 616-627, 2024.

[32] Tagata, T. et al.: Forming Limit Diagram for a Superplastic 5083 Aluminum Alloy, Materials Transactions, Vol. 45, No. 8, pp. 2516-2520, 2004.

[33] Jarrar, F.S. et al.: Simulation of High-Temperature AA5083 Bulge Forming with a Hardening/Softe–ning Material Model, Journal of Materials Engi–neering and Performance, Vol. 18, No. 7, pp. 863-870, 2009.


## NOMENCLATURE

| | |
|---|---|
| A | Initial yield stress |
| AR | Die aspect ratio |
| B | Hardening constant |
| C | Strain-rate sensitivity coefficient |
| D | Damage parameter |
| $D_1$-$D_5$ | Johnson–Cook damage constants |
| E | Young's modulus |
| m | Thermal softening exponent |
| n | Strain hardening exponent |
| t | Current sheet thickness |
| $t_0$ | Initial sheet thickness |
| $t_f$ | Time necessary to reach a target strain value |
| T | Temperature |
| $T_m$ | Melting temperature |
| $T_0$ | Room temperature |

### *Greek symbols*

| | |
|---|---|
| $\sigma$ | Equivalent flow stress |
| $\dot{\varepsilon}$ | Equivalent strain rate |
| $\dot{\varepsilon}_0$ | Reference strain rate |
| $\varepsilon_1$ | Major strain |
| $\varepsilon_2$ | Minor strain |
| $\varepsilon_f$ | Fracture strain |
| $\Delta\varepsilon_p$ | The increment of accumulated plastic strain |

### *Abbreviations*

| | |
|---|---|
| PBF | Pneumatic bulge forming |
| PBT | Pneumatic bulge test |
| FE | Finite element |
| JC | Johnson-Cook |
| FLD | Forming Limit Diagram |
| LVDT | Linear Variable Differential Transformer |
| PEEQ | Equivalent Plastic Strain |
| STH | Sheet thickness |
| ASTM | American Society for Testing and Materials |

## ПОНАШАЊЕ ДЕФОРМАЦИЈЕ И УСЛОВИ ОТКАЗА ПРИ ПНЕУМАТСКОМ ОБЛИ–КОВАЊУ ИЗБОЧИНА ПОМОЋУ КРУЖНИХ И ЕЛИПТИЧНИХ КАЛУПА


**С.Х. Али, А.О. Балод, А.Х. Џасим**



Понашање деформације и отказа алуминијумског лима АА1050 током топлог пнеуматског облико–вања избочина (PBF) испитано је експериментално и нумерички коришћењем кружних и елиптичних калупа. Симулације су извршене у Abaqus/Explicit коришћењем Johnson-Cook (JC) модела на 300 °C под константним нивоима притиска.

Резултати су показали да однос ширине и висине калупа има снажан утицај на деформацију и отказ. Кружни калуп је довео до равномерније двоосне деформације и велике висине куполе, док су елиптични калупи изазвали неравномерну дефор–мацију и локализацију напрезања дуж главне осе. До отказа је дошло у подручју максималног истањи–вања, где се пукотина протезала дуж главне осе. Пукотина је била мала и налазила се на врху куполе у кружном калупу, док је у елиптичним калупима постајала дужа и продужена. Формабилност се побољшавала са повећањем дебљине лима (STH) од 0,7 mm до 1 mm, омогућавајући веће напрезање и висину куполе пре отказа.